*Supernova 1987A:30 years later - Cosmic Rays and Nuclei from Supernovae and their aftermaths*
*Proceedings IAU Symposium No. 331, 2017*
*A. Marcowith, M. Renaud, G. Dubner, A. Ray & A. Bykov, eds.*


doi:10.1017/S174392131700446X

# Multimessenger Predictions from 3D General-Relativistic Core-Collapse Supernovae Models

**Kei Kotake[1], Takami Kuroda[2] and Kazuhiro Hayama[3]**

[1]Department of Applied Physics, Fukuoka University, Jonan, Nanakuma, Fukuoka 814-0180, Japan,

[2]Institute of Kernphysik, Technische Universtät Darmstadt, D-64289 Darmstadt, Germany,

[3]Institute for Cosmic Ray Research, University of Tokyo, 5-1-5 Kashiwa-no-Ha, Kashiwa City, Chiba 277-8582, Japan

**Abstract.** In this contribution, we present results from fully general-relativistic three-dimensional (3D) simulations of a non-rotating $15M_{\odot}$ star using different nuclear equations of state (EOSs). We show that the SASI (standing-accretion-shock-instability) activity occurs much more vigorously in models with softer EOS. By performing detailed analysis of the gravitational-wave (GW) emission, we find a new GW signature that is produced predominantly by the SASI-induced downflows to the proto-neutron star. We discuss the detectability of the GW signal by performing a coherent network analysis where multiple detectors including LIGO Hanford, LIGO Livingston, VIRGO, and KAGRA are considered. We point out that the GW signal, whose typical frequency is in the best sensitivity range of the laser-interferometers, could potentially provide the *live broadcast* that pictures how the supernova shock is dancing in the core. The detection horizon of the signal is estimated as 2∼3 kpc for the current generation detectors, which can extend up to ∼100 kpc for the third generation detectors like Cosmic Explorer. We furthermore perform a correlation analysis between the SASI-modulated GW and neutrino signals. Our results show that the time correlation of the two signals becomes highest when we take into account the travel timescale of adverting material from the (average) neutrino-sphere to the proto-neutron star surface.

**Keywords.** supernovae:general, hydrodynamics, instabilities, neutrinos, gravitational waves

## 1. Introduction

Accumulating observational evidence from precise, multi-wavelength electromagnetic-wave (EM) observations of ejecta morphologies, spatial distributions of nucleosynthetic yields have all pointed towards core-collapse supernovae (CCSNe) being generally aspherical (e.g., Maeda *et al.*(2008), Grefenstette *et al.* (2015), Tanaka *et al.* (2017) and references therein). Unquestionably important as these discoveries are, these EM signals are secondary for probing the multidimensionality inside the supernova engine because they are only able to provide images of optically thin regions far away from the central core.

Much more direct information is delivered to us by neutrinos and gravitational waves (GWs). This year is 30 years after SN1987A, which has opened up neutrino astronomy (Hirata *et al.* (1987)). In 2015, the centurial year after Einstein's theory of general relativity (GR), the twin detectors of the Laser Interferometer Gravitational-wave Observatory (LIGO) coined the *first direct detection* of GWs. It turns out that this (potentially) Nobel Prize-winning event is produced by the merger of two black holes (Abbott *et al.* (2016)).

The second generation detectors like KAGRA (Aso *et al.* (2013)), advanced VIRGO (Hild *et al.* 2009) will be on-line in the coming years. Next to compact binary mergers, CCSNe are among one of the most promising astrophysical sources of GWs (e.g., Kotake (2013) for reviews).

From a theoretical point of view, understanding the origin of the explosion multi-dimensionalities is also indispensable for clarifying the yet uncertain CCSN mechanisms. After a half-century of continuing efforts, theory and neutrino radiation-hydrodynamics simulations are now converging to a point that multi-dimensional hydrodynamics instabilities play a pivotal role in the neutrino mechanism (Bethe (1990)), the most favoured scenario to trigger explosions. In fact, a number of self-consistent simulations in two or three spatial dimensions (2D, 3D) now report shock revival of the stalled bounce shock into explosion by the neutrino mechanism. These successful models have strengthened our confidence in the multi-D neutrino-driven paradigm (see Müller (2016), Janka *et al.* (2016), Foglizzo *et al.* (2015), Burrows (2013), Kotake *et al.* (2012) for recent reviews).

In this contribution, we present results of 3D-GR simulations of a non-rotating $15M_{\odot}$ star using two representative EOSs based on our recent work (Kuroda *et al.* (2016)). We start to briefly summarize our numerical method for GR-radiation hydrodynamics and initial models in Section 2. In Section 3, we report results, which includes new analysis on the neutrino emission from the 3D-GR models and the correlation analysis between the SASI-modulated neutrino and GW signals.

## 2. Numerical Method and Initial Models

In our full GR radiation-hydrodynamics simulations, the evolution equations of metric, hydrodynamics are solved based on the BSSN formalism (Shibata and Nakamura (1995), Baumgarte and Shapiro (1999)) and the evolution of neutrino radiation field based on the M1 scheme (see collective references in Kuroda *et al.* (2012), Kuroda *et al.* (2014)). To follow the 3D hydrodynamics up to $\lesssim 400$ ms postbounce, we shall omit the energy dependence of three-flavor neutrino radiation fields in this work (see, however, the multi-energy transport scheme in Kuroda *et al.* (2016)).

We employ a frequently used 15 $M_{\odot}$ star of Woosley and Weaver (1995). The 3D computational domain (15000 km width) consists of nested cubic boxes with the minimum grid size near the origin being $\Delta x = 458$m (the effective angular resolution is $\sim 1^{\circ}$). We use two kinds of EOSs based on different nuclear interaction treatments, which is TM1 of Hempel and Schaffner-Bielich (2010) and SFHx of Steiner *et al.* (2013). We label the two models simply by the EOS used (SFHx or TM1). From the mass-radius relation of a cold neutron star (NS), the maximum gravitational mass and the radius is $M_{\rm max} =$ 2.1 and 2.2 $M_{\odot}$, $R = 12$ and 14.5 km for SFHx and TM1, respectively (Fischer *et al.* (2014)). Note that SFHx is softer than TM1 because of its smaller NS radius and mass relative to TM1.

Extraction of GWs is done by the conventional quadrupole formula (Misner *et al.* (1973)), in which the transverse and the traceless gravitational field $h_{ij}$ is expressed as,

$$h_{ij}(\theta,\phi) = \frac{A_{+}(\theta,\phi)e_{+} + A_{\times}(\theta,\phi)e_{\times}}{D}. \tag{2.1}$$

In Eq.(2.1), $A_{+/\times}(\theta,\phi)$ represent amplitude of orthogonally polarized wave components with emission angle $(\theta,\phi)$ dependence, $e_{+/\times}$ denote unit polarization tensors and $D$ is the source distance where we set $D = 10$ kpc in this contribution, unless otherwise stated.

https://doi.org/10.1017/S174392131700446X Published online by Cambridge University Press

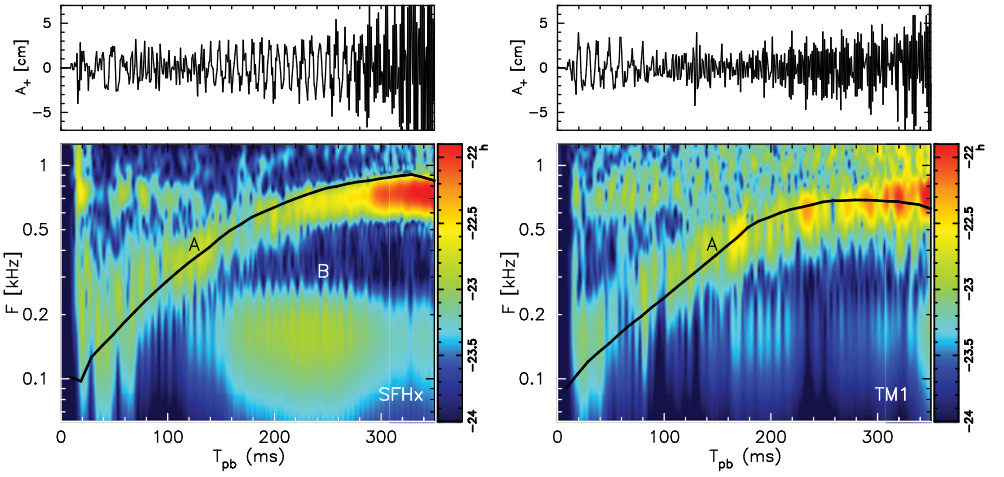


**Figure 1.** In each set of panels, we plot, top; gravitational wave amplitude of plus mode $A_+$ [cm] (black), bottom; characteristic wave strain in frequency-time domain $\tilde{h}$ in a logarithmic scale which is over plotted by the expected peak frequency $F_{\rm peak}$ (black). Left and right panels are for SFHx and TM1, respectively.

## 3. Results from 3D GR Simulations of a Non-rotating 15 $M_\odot$ Star

### 3.1. *3D hydrodynamics and GW signatures*

Figure 1 shows time evolution of the GW amplitude (only plus mode is shown $A_+(\theta,\phi)$, black line) in the top panel and the characteristic wave strain in time-frequency domain $\tilde{h}(\theta,\phi,F)$ (see Eq.(44) in Kuroda *et al.* (2014)) in the bottom panel. Here $F$ denotes the GW frequency. We extract GWs along the north pole $(\theta,\phi)=(0,0)$ because the GW amplitude is less sensitive to the viewing angle.

The GW amplitude ($A_+$, upper two panels) shows a consistent behavior as reported in Müller *et al.* (2013), Andresen *et al.* (2016), and Yakunin *et al.* (2017). It shows initial low frequency and slightly larger amplitude till $T_{\rm pb}\sim 60$ ms ($T_{\rm pb}$ represents postbounce time), which comes from the so-called prompt convection. This is followed by a quiescent phase with higher frequency till $T_{\rm pb}\sim 150$ ms. Afterward the amplitude and frequency become larger with time as non-sphericity of fluid motion becomes chaotically bigger with the growth of neutrino-driven convection and the SASI.

From the GW spectrograms (bottom panels in Figure 1), we see a narrow band spectrum (labeled as "A" in both models) which shows an increasing trend in its peak frequency. As previously identified (Müller *et al.* (2013), Murphy *et al.* (2009)), this peak shift can be explained by properties of PNS, such as its compactness and surface temperature. By following Eq.(17) in Müller *et al.* (2013), we superimpose $F_{\rm peak}$ in the bottom panels of Figure 1 (black line). One can see that in both models, $F_{\rm peak}$ indeed tracks spectral peak quite well, although there is some exception in late phase of SFHx ($T_{\rm pb}\gtrsim 200$ ms) when the other strong component appears at $100\lesssim F\lesssim 200$ Hz (labeled as "B"). The component "A" is thus actually originated from the $g$-mode oscillation of the PNS surface.

Before going into detail to explain the origin of the (low-frequency) component "B", we touch on several key differences in the hydrodynamics evolution between SHFx and TM1. Figure 2 shows that SFHx experiences violent sloshing (top left) and spiral motions of the SASI (top right), before neutrino-driven convection dominates over the SASI (bottom

https://doi.org/10.1017/S174392131700446X Published online by Cambridge University Press

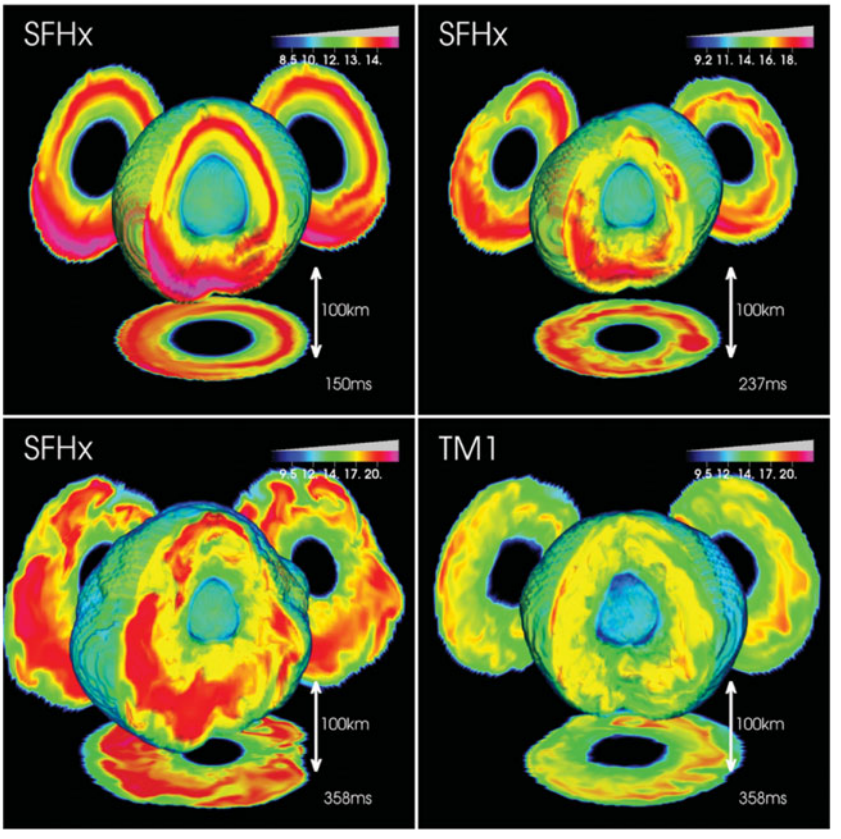


**Figure 2.** Snapshots of the entropy distribution ($k_{\rm B}$ baryon$^{-1}$) for models SFHx and TM1 (top left; $T_{\rm pb}$ = 150 ms of SFHx, top right; $T_{\rm pb}$ = 237 ms of SFHx, bottom left; $T_{\rm pb}$ = 358 ms of SFHx, bottom right; $T_{\rm pb}$ = 358 ms of TM1). The contours on the cross sections in the $x = 0$ (back right), $y = 0$ (back left), and $z = 0$ (bottom) planes are, respectively projected on the sidewalls of the graphs. The 90° wedge on the near side is excised to see the internal structure. Note that to see the entropy structure clearly in each dynamical phase, we change the maximum entropy in the colour bar as $s_{\rm max}$ = 16, 20 and 22 $k_{\rm B}$ baryon$^{-1}$ for $T_{\rm pb}$ = 150, 237 and 358 ms, respectively.

left), whereas the SASI activities are less developed in TM1. For SFHx, the clear SASI motions are observed after the prompt convection phase ceases at $T_{\rm pb} \sim 50$ ms.

So how are these hydrodynamical evolutions related to the GW emission "B" in Fig. 1 ? For clarity, we present a back-of-the-envelope estimation of the GW amplitude as

$$D|h| \sim 2\epsilon M R^2/T_{\rm dyn}^2 \sim 2\epsilon M^2/R \sim 2\epsilon R^2 \dot{M}^2/M, \tag{3.1}$$

where $M$, $R$ and $T_{\rm dyn}$ represent the mass, size and dynamical time scale of the system, respectively, in the geometrized unit. Here we have used the following reasonable assumptions

$$T_{\rm dyn} \sim M/\dot{M} \tag{3.2}$$

or

$$T_{\rm dyn} \sim R/V \sim \sqrt{R^3/M}, \tag{3.3}$$

with $V \sim \sqrt{M/R}$ being the velocity derived by the energy conservation. From the last

https://doi.org/10.1017/S174392131700446X Published online by Cambridge University Press

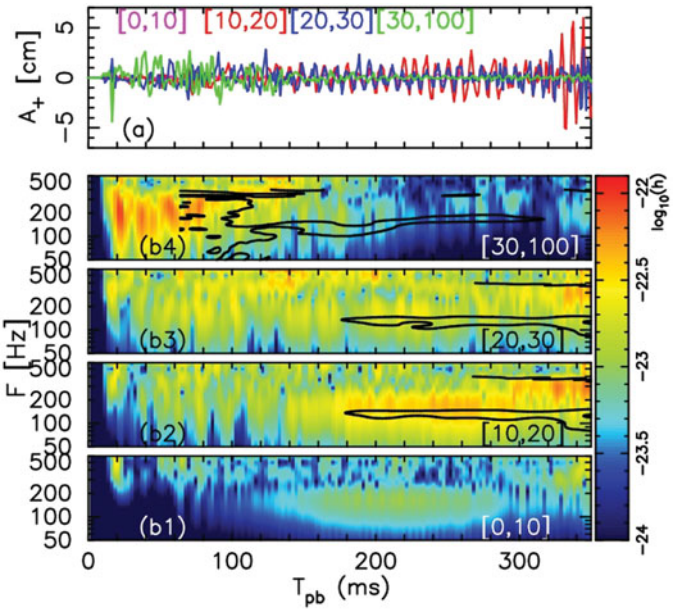


**Figure 3.** Rough measurement of contribution from each spherical shell to (a) the GW amplitude and (b1-4) their spectrogram $\tilde{h}$ in a logarithmic scale. We show the contributions from four spherical shells with interval of [0,10], [10,20], [20,30] and [30,100] km. Black contours over plotted on spectrograms for $\tilde{h}$ represent half maximum of spectrograms for mass accretion rate measured at $R = 17$ km (panel b2), 23 km (panel b3), and 48 km (panel b4).

relation in Eq.(3.1), we expect that significant time variation in the mass accumulation onto the PNS can potentially lead to the GW emission.

In Figure 3, we superimpose spectrogram of the mass accretion rate $\dot{M}(R)$ (the black contour at half maximum) measured at $R = 17$, 23, and 48 km on top of the GW spectrogram. While $\dot{M}(R = 48\text{km})$ starts quasi-periodic oscillation at $F \sim 100 - 200$Hz around $T_{\rm pb} \sim 120$ ms, we find a time delay of $\sim 60$ ms for their appearance at deeper region ($R = 17$ and 23 km). Since the density averaged mean radial velocity between the lepton driven ($10 \lesssim R \lesssim 20$ km) and the entropy driven ($R \gtrsim 40$ km) convection layers is $\sim 5 \times 10^7$ cm s$^{-1}$, the time delay is consistent with the advection time scale over the stable layer ($20 \lesssim R \lesssim 40$ km). Furthermore, coincidence of time modulation in $\dot{M}(R)$ and the GW component "B" is obvious from panel (b2).

Finally, we are trying to connect the SASI activities with the GW component B. Figure 4 shows spectrograms of normalized mode amplitude of the sloshing-SASI mode $|\tilde{A}_{10}|$, the mass accretion rate $|\tilde{\dot{M}}|$ measured at $R = 17$ km, normalised quadrupole deformation of the isodensity surface $\tilde{\epsilon}_l$ for $l = 2$. As a guide to measure the GW energy spectrum, $\tilde{\epsilon}_l$ denotes a Fourier component of normalised mode amplitude $\epsilon_l$ defined by

$$\epsilon_l \equiv \sqrt{\sum_{m=-l,l} \left(R^{14}_{l,m}\right)^2} / R^{14}_{0,0} \ , \tag{3.4}$$

where $R^{14}_{l,m}$ is evaluated by the spherical polar expansion of the isodensity surface $R^{14}$ extracted at $\rho = 10^{14}$ g cm$^{-1}$ as the same way as for the shock surface. Although several other modes are excited at the surface, only the leading contribution ($l = 2$ mode) to the GW emission is shown in the panel. As a reference, the isodensity surface $R^{14}$ locates $\sim 13.5$ km during $150 \lesssim T_{\rm pb} \lesssim 300$ ms in SFHx. From the last relation in Eq.(3.1), we

https://doi.org/10.1017/S174392131700446X Published online by Cambridge University Press

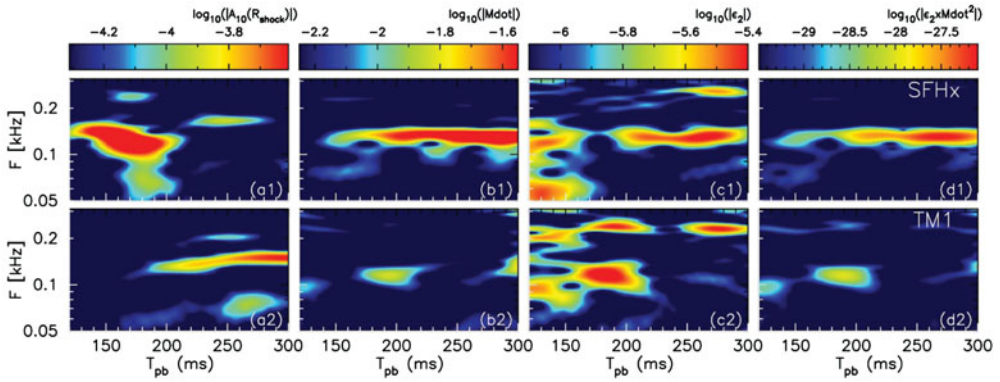


**Figure 4.** Spectrograms of; (a) Fourier decomposed normalized mode amplitude $|\tilde{A}_{10}|$ of the shock surface for the sloshing-SASI mode, (b) the mass accretion rate $\dot{M}$ (with a dimension of $M_\odot$), through surface of a sphere with radius of $R = 20$ km, (c) deformation of the isodensity surface $\tilde{\epsilon}_l$ for $l = 2$ mode and (d) a rough measurement of the GW energy spectrum which is proportional to $\sim \epsilon R^2 \dot{M}^2 M^{-1}$ (see text). Top and bottom rows are for SFHx and TM1, respectively.

plot $\log_{10}|h| \sim \log_{10} \epsilon \dot{M}^2 + \text{const.}$ in panels (d) of Fig. 4 with assuming $M = 0.5 M_\odot$, a mass contained in $10 \lesssim R \lesssim 20$ km, and $R^{14} = 13.5$ km stay nearly constant.

During $140 \lesssim T_{\rm pb} \lesssim 180$ ms in SFHx, we see a strong sloshing motion which has its peak frequency at $100 \lesssim F \lesssim 200$ Hz (a1). With some time delay ($\sim 50$ ms) from the appearance of it, the mass accretion rate $\dot{M}$ starts showing a quasi-periodic oscillation at the same frequency range $100 \lesssim F \lesssim 200$ Hz (b1) and it excites oscillation on the isodensity surface (c1). A combination of large $\dot{M}$ and $\epsilon_2$ expect GW emissions appearing in panel (d1) and it can well explain the feature in Figure 1. During $200 \lesssim T_{\rm pb} \lesssim 300$ ms, $\epsilon_2$ stays $\sim 3 \times 10^{-4}$ in SFHx. A rough measurement of the GW amplitude due to this deformation, $A \sim 2\epsilon_2 M^2 R^{-1}$, deduces $A \sim 2$ cm which is consistent with the actual amplitude (Figure 3).

### 3.2. *Detectability of the SASI-induced GW signals*

As we have discussed above, the GW spectrogram is characterized by the two components, which comes from the high-frequency g-mode PNS (surface) oscillation (e.g., A in Figure 1, hereafter we shortly call it shortly as "g-mode" GW) and from the low-frequency ($100 \sim 200$ Hz) SASI-induced downflows (e.g., B in Figure 1, we call it as "SASI-mode" GW). In order to discuss detectability of the two distinct features in the spectrogram, we perform a coherent work analysis where multiple detectors including LIGO Hanford, LIGO Livingston, VIRGO, and KAGRA are considered (e.g., Hayama *et al.* (2015) for more details).

The left panel of Figure 5 shows the spectrogram of the reconstructed waveform of SFHx at a distance of 3 kpc. Setting an optimal threshold of detection as 10 (see the color scale), one could see that the g-mode GW in the fully non-linear phase (at $T_{\rm pb} \sim 350$ ms) is most likely to be detectable, whereas the SASI-mode GW (in the low-frequency range) is second largest (compare the (pre-processed) original spectrogram in Figure 1 (left panel)). Our results suggest that LIGO-class detectors could marginally detect and hopefully differentiate the two signatures (g-mode vs. SASI-mode GWs) only for a very close-by event (a few kpc). But with the advent of the third generation detectors (right panel of Figure 5), the detection horizon is expected to extend up to 100 kpc (out to LMC). For a *Galactic* source, the prompt convection (red region $T_{\rm pb} \lesssim 50$ ms),

https://doi.org/10.1017/S174392131700446X Published online by Cambridge University Press

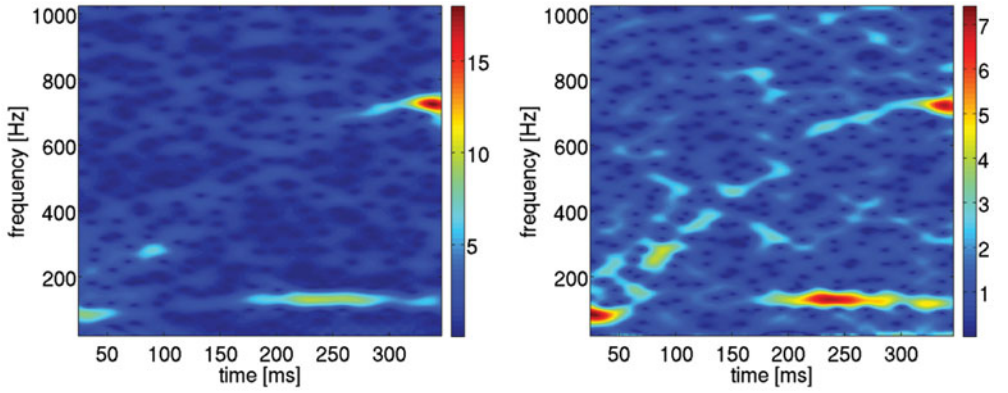


**Figure 5.** The left panel is the spectrogram of the reconstructed waveform of SFHx at a distance of 3 kpc. The color scale represents the signal-to-noise ratio (SNR) in the spectrogram (e.g., $\mathrm{SNR}_{\mathrm{TF}}$, see the definition in Hayama *et al.* (2015)). The right panel is similar to the left panel but the distance to the source is taken as 100 kpc and the design sensitivity of Cosmic Explore (Abbott *et al.* (2017)) is also included in the coherent network analysis.

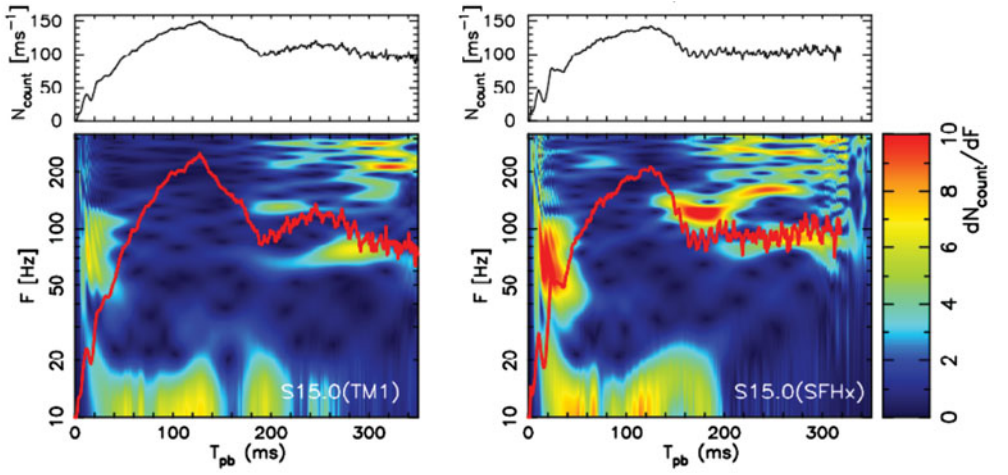


**Figure 6.** The top panel shows detection rate of $\bar{\nu}_e$ for TM1 (left panel) and SFHx (right panel) in Hyper-Kamiokande at 10 kpc. The bottom panel shows the spectrogram where the detection rate is superimposed by the red line.

the running-up of the g-mode GW, and the SASI-induced island (red region at $200 \lesssim T_{\mathrm{pb}} \lesssim 300$ ms) might be clearly visible by the third generation detectors as if it were the noise-free theoretical spectrogram (e.g., Figure 1 (left panel)).†

### 3.3. *SASI-induced Modulation in Neutrino Signals*

Figure 6 shows detection rate of anti-electron neutrino events ($\bar{\nu}_e$) at (the future) Hyper-Kamiokande (Hyper-K)(Abe *et al.* (2011)). Here the fiducial volume of Hyper-K is taken as 440 kton. Note that from the fiducial volume of Super-K (32 kton), one can get the number in Super-K from Figure 6.

As previously identified (Tamborra *et al.* (2013)), the SASI-induced signal modulation is both seen in the top panels of Figure 6. Reflecting the stronger SASI activity in SFHx

† The Cosmic Explore is proposed to start operation in the 2030's (https://dcc.ligo.org/public/0120/T1500290/003/T1500290.pdf).

https://doi.org/10.1017/S174392131700446X Published online by Cambridge University Press

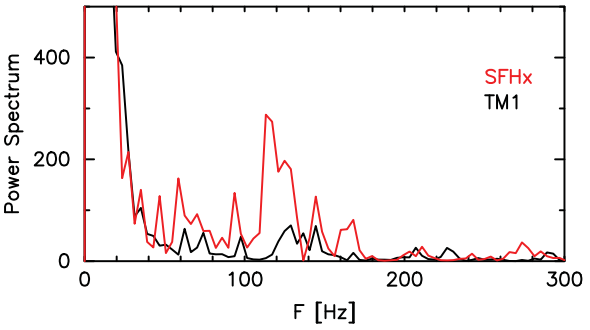


**Figure 7.** Power spectrum of the IceCube neutrino ($\bar{\nu}_e$) event rate on the time window of 0 - 300 ms postbounce for SFHx (red line) and TM1 (black line). The source is assumed at a distance of 10 kpc. The shot noise caused by the background of IceCube of $1.5 \times 10^3$ ms$^{-1}$ is assumed (e.g., Tamborra *et al.* (2014)).

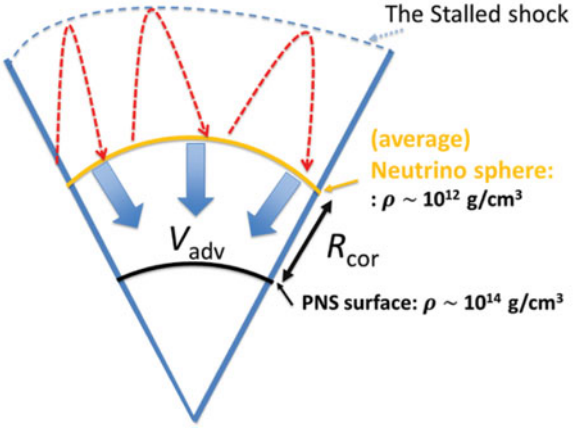


**Figure 8.** Schematic drawing to illustrate the different radial positions of SASI-induced neutrino and GW emission in the postbounce core. Below the stalled shock (dashed blue line, labeled as "The stalled shock"), non-spherical flows (red line with arrow) hit first the (average) neutrino sphere then penetrates into the PNS surface. $R_{\rm cor}$ represents the distance between the neutrino sphere ($\bar{\nu}_e$ in this case) and the PNS. $V_{\rm adv}$ is the typical velocity of the downflows there.

(right panel) compared to TM1 (left panel), more clearer excess (bottom panels) is seen for SFHx in the frequency range of 100 - 200 Hz in accordance with the SASI-modulation (red thick line). Note that the detection rate in Figure 6 is angle-averaged one. If one could take into account the viewing angle correction, the modulation amplitude could become more pronounced as shown in Tamborra *et al.* (2014).

IceCube by its superior statistics compared to Hyper-K could help differentiate smaller modulation amplitudes in the two models. In fact, Figure 7 supports this, where one can see the more pronounced peak for SFHx (red line) compared to TM1 (black line).

### 3.4. *Correlation between SASI-induced GW and Neutrino Signals*

From Figures 1 and Figure 7, one can see that both of the modulation frequency of the GW and neutrino signals is relatively close (i.e., in the range of 100 $\sim$ 200 Hz). Is there any correlation between them ? Figure 8 illustrates how the two signals could have a correlation. During the simulation timescale, the radial distance ($R_{\rm cor}$) between the neutrino sphere and the PNS can be crudely estimated as 50 km, and $V_{\rm adv}$ as $10^8$ cm/s,

https://doi.org/10.1017/S174392131700446X Published online by Cambridge University Press

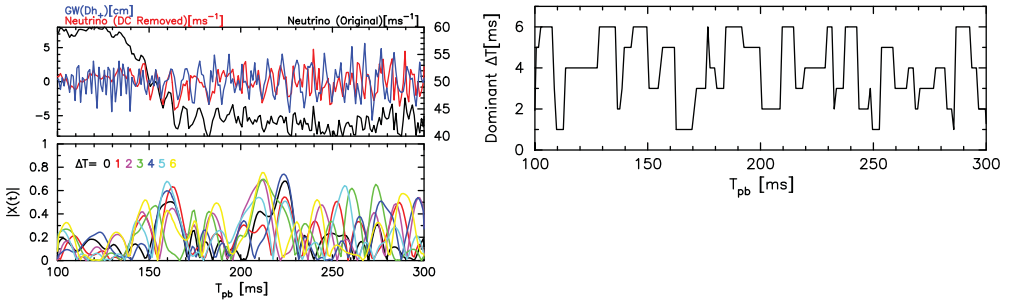


**Figure 9.** The left panel (*top*) shows the gravitational waveform ($h(t)$, blue line) and the neutrino count rate ($n_\nu(t)$, red line at Hyper-K), where the count rate with the DC component is also shown (black line) as a reference. The left-bottom panel shows the correlation coefficient $0 \leqslant X(t) \leqslant 1$ between the two signals (top panel, blue and red curves) when we shift the time of the two waveforms by $\Delta T$ (ms) ($X(t) \equiv \langle h(t+\Delta T) n_\nu(t) \rangle$). Note $\Delta T = 0$ means that we take the correlation using the data in the top panel. The right panel shows the evolution of $\Delta T$ where the correlation becomes maximum at a given time.

then the timescale of downflows travelling from the neutrino-sphere to the PNS reads $\Delta T \sim R_{\rm cor}/V_{\rm adv} \sim 5$ ms.

Figure 9 shows that the correlation between the SASI-modulated neutrino and GW signals (left panels) takes maximum for the time delay of $\Delta t = 4 \sim 6$ ms (right panel), which fits well with the schematic understanding in Figure 8. More careful analysis is apparently needed if we could or could not distinguish the signal modulation from noises. But if it could be possible, we could extract the information regarding the distance ($R_{\rm cor}$ in Figure 8) from the neutrino-sphere and the PNS, which is otherwise very hard to measure by other means.

## 4. Perspectives; where are we going ?

First we need to investigate the dependence of numerical resolution on the presented results. For enhancing the predictive power of the multi-messenger predictions, we have to upgrade from the gray to multi-energy neutrino transport including more detailed neutrino opacity (Kotake *et al.* in preparation). Here we have only presented a snapshot of our continuing endeavour for making more precise multi-messenger predictions based on more sophisticated 3D-GR models.

We are thankful to stimulating discussions/conversations with R. Diehl, H.T. Janka, G. Raffelt, C. Fryer, A. Heger, R. Hirshi, S. Katsuda, A. Wongwathanarat, E. O'Connor, J. Guilet, and R. Kazeroni during the conference. This study was supported by JSPS (Nos. 24244036, 26707013 and 26870823) and by MEXT (Nos. 15H00789, 15H01039, 15KK0173) and JICFuS as a priority issue to be tackled by using Post 'K' Computer.

## References

Abe, K., Abe, T., Aihara, H., *et al.* 2011, arXiv:1109.3262
Abbott, B. P., Abbott, R., *et al.* 2016, *Physical Review Letters*, 116, 061102
Abbott, B. P., *et al.* 2017, *Classical and Quantum Gravity*, 34, 044001
Aso, Y., Michimura, Y., Somiya, K., *et al.* 2013, *Phys. Rev. D*, 88, 043007
Andresen, H., Mueller, B., Mueller, E., & Janka, H.-T. 2016, arXiv:1607.05199
Baumgarte, T. W. & Shapiro, S. L. 1999, *Phys. Rev. D*, 59, 024007
Bethe, H. A. 1990, *Reviews of Modern Physics*, 62, 801
Burrows, A. 2013, *Reviews of Modern Physics*, 85, 245

https://doi.org/10.1017/S174392131700446X Published online by Cambridge University Press

Fischer, T., Hempel, M., *et al.* 2014, *European Physical Journal A*, 50, 46
Foglizzo, T., Kazeroni, R., Guilet, J., *et al.* 2015, *Publications of the Astron. Soc. of Australia*, 32, e009
Grefenstette, B. W., Reynolds, S. P., Harrison, F. A., *et al.* 2015, *ApJ*, 802, 15
Hayama, K., Kuroda, T., Kotake, K., & Takiwaki, T. 2015, *Phys. Rev. D*, 92, 122001
Hempel, M. & Schaffner-Bielich, J. 2010, *Nuclear Physics A*, 837, 210
Hild, S., Freise, A., Mantovani, M., *et al.* 2009, *Classical and Quantum Gravity*, 26, 025005
Hirata, K., Kajita, T., Koshiba, M., Nakahata, M., & Oyama, Y. 1987, *Physical Review Letters*, 58, 1490
Janka, H.-T., Melson, T., & Summa, A. 2016, *Annual Review of Nuclear and Particle Science*, 66, 341
Kotake, K., Sumiyoshi, K., Yamada, S., *et al.* 2012, *Progress of Theoretical and Experimental Physics*, 2012, 01A301
Kotake, K. 2013, *Comptes Rendus Physique*, 14, 318
Kuroda, T., Kotake, K., & Takiwaki, T. 2012, *ApJ*, 755, 11
Kuroda, T., Takiwaki, T., & Kotake, K. 2014, *Phys. Rev. D*, 89, 044011
Kuroda, T., Takiwaki, T., & Kotake, K. 2016, *ApJS*, 222, 20
Kuroda, T., Kotake, K., & Takiwaki, T. 2016, *ApJL*, 829, L14
Maeda, K., Kawabata, K., Mazzali, P. A., *et al.* 2008, *Science*, 319, 1220
Misner, C. W., Thorne, K. S., & Wheeler, J. A. 1973, Gravitation
Müller, B. 2016, *Publications of the Astron. Soc. of Australia*, 33, e048
Müller, B., Janka, H.-T., & Marek, A. 2013, *ApJ*, 766, 43
Murphy, J. W., Ott, C. D., & Burrows, A. 2009, *ApJ*, 707, 1173
Shibata, M. & Nakamura, T. 1995, *Phys. Rev. D*, 52, 5428
Steiner, A. W., Hempel, M., & Fischer, T. 2013, *ApJ*, 774, 17
Takiwaki, T., Kotake, K., & Suwa, Y. 2016, *MNRAS*, 461, L112
Tamborra, I., Hanke, F., Müller, B., Janka, H.-T., & Raffelt, G. 2013, *Physical Review Letters*, 111, 121104
Tamborra, I., Raffelt, G., Hanke, F., Janka, H.-T., & Müller, B. 2014, *Phys. Rev. D*, 90, 045032
Tanaka, M., Maeda, K., Mazzali, P. A., Kawabata, K. S., & Nomoto, K. 2017, *ApJ*, 837, 105
Woosley, S. E. & Weaver, T. A. 1995, *ApJS*, 101, 181
Yakunin, K. N., Mezzacappa, A., Marronetti, P., *et al.* 2017, arXiv:1701.07325

## Discussion

JANKA: In your plot showing the SNR (signal-to-noise ratio) as a function of distance (not shown in this contribution), the GW detection horizon extends out to 10 kpc. But the SASI-modulated signature (Figure 5 (left panel)) can be seen only visible to 2∼3 kpc. What is the different between the two statements ?

KOTAKE: This is an important question. Let me first clarify this. The first plot you are mentioning is the so-called *optimal* SNR where the matched filtering method is employed using the GW signals over the entire simulation time. On the other hand, the SNR on the spectrogram (Figure 5 (left)) is estimated only over the time when the SASI activity is active, and the SNR is estimated after the signal reconstruction. So the SNR becomes much smaller compared to the optimal SNR.

JANKA: I'm asking this because we have also a paper by Andresen *et al.* (2016), where we pointed out that the detection horizon of the SASI-modulated GW signal is a few kpc by the currently running detectors.

KOTAKE: All right. So, our results are consistent in this regard.

https://doi.org/10.1017/S174392131700446X Published online by Cambridge University Press